

# Aperture Synthesis CO( $J = 1-0$ ) Observations and Near-Infrared Photometry of the Non-Barred Seyfert Galaxy NGC 5033

Kotaro KOHNO

*Institute of Astronomy, The University of Tokyo, 2-21-1, Osawa, Mitaka, Tokyo 181-0015*

*kkohno@ioa.s.u-tokyo.ac.jp*

Baltasar VILA-VILARÓ

*Steward Observatory, The University of Arizona, Tucson, AZ 85721, U.S.A.*

*bvila@as.arizona.edu*

Seiichi SAKAMOTO, Ryohei KAWABE, and Sumio ISHIZUKI

*National Astronomical Observatory of Japan, 2-21-1, Osawa, Mitaka, Tokyo, 181-8588*

*seiichi@nro.nao.ac.jp, kawabe@nro.nao.ac.jp, ishizksm@cc.nao.ac.jp*

and

Satoki MATSUSHITA

*Harvard-Smithsonian Center for Astrophysics,  
60 Garden St., MS 78, Cambridge, MA 02138, U.S.A.  
smatsushita@cfa.harvard.edu*

(Received 2002 May 24; accepted 2002 December 27)

## Abstract

Aperture synthesis observations of CO( $J = 1-0$ ) emission and near-infrared broad-band photometry of the non-barred Seyfert galaxy NGC 5033 ( $D = 18.7$  Mpc) were performed. Our  $3''.9 \times 3''.6$  resolution CO observations reveal a perturbed distribution and the kinematics of molecular gas in the center of NGC 5033; we find the characteristic gaseous features that are widely observed in barred spiral galaxies, such as two bright CO peaks near the center (separated by  $\sim 3''$  or 270 pc from the nucleus), two offset ridges of CO emission emanating from the CO peaks, and a CO ring (with a radius of  $\sim 14''$  or 1.3 kpc). Double-peaked velocity profiles are also evident near the two CO peaks, implying that these CO peaks are orbit crowding zones in a barred/oval potential. Although NIR data only give an upper limit of the possible bar lengths, due to a large inclination of the NGC 5033 disk ( $i = 68^\circ$ ), our CO data clearly suggests the presence of a small (the semi-major axis of about  $12'' - 15''$  or 1.1 – 1.4 kpc) nuclear bar (or oval structure) in the center of the “non-barred” galaxy NGC 5033. Our results demonstrate that high-resolution CO imaging-spectroscopy is useful to search for nuclear bars, even in highly inclined systems where isophoto fitting techniques are not applicable. We find that the gas mass-to-dynamical mass ratio,  $M_{\text{gas}}/M_{\text{dyn}}$ , is small ( $\leq 1\%$ ) within a radius of  $2''$  or 180 pc, in contrast to starburst nuclei. This implies that the starburst does not cohabitate in the type-1.5 Seyfert nucleus of NGC 5033.

**Key words:** galaxies: active — galaxies: individual(NGC 5033) — galaxies: ISM — galaxies: Seyfert — galaxies: structure

## 1. Introduction

Active galactic nuclei (AGNs) are widely believed to be powered by accretion onto super-massive black holes (SMBHs). Recent observational studies of galaxies have revealed that substantial numbers of galaxies do contain SMBHs in their nuclei (e.g., Kormendy, Richstone 1995; Ho 1999; van der Marel 1999); SMBHs are also found even in quiescent galaxies, such as the Milky Way (e.g., Eckart, Genzel 1996). These facts prompt us to argue that many (or most) quiescent galaxies were active in the past. It is therefore essential to investigate the fueling process in order to understand the nature of AGNs, particularly the difference between *active* and *starving* nuclei.

A promising fuel source is molecular gas, because it dominates the interstellar matter (ISM) in the circumnuclear regions (kilo-parsec scale) of many spiral galaxies. It is, however, not obvious how it could be transported from typical galactic radii ( $\sim 10$  kpc) down to the scale of the central engine ( $\leq 1$  pc). Galactic bars are frequently invoked as candidates for facilitating the transfer of mass in a host of active galaxies (e.g., Shlosman et al. 1989). In fact, the bar-driven gas structures can be widely seen in many Seyfert galaxies (e.g., Helfer, Blitz 1995; Kohno et al. 1999b; Baker 1999; Maiolino et al. 2000; Schinnerer et al. 2000; Kohno et al. 2001; Koda et al. 2002). There appears, however, observational evidence *against* the bar-induced fueling scenario as well. Ho et al. (1997c) have reported that galaxies hosting AGNs do not appear to be significantly affected by the presence of a bar, based on their extensive

optical spectroscopic survey of 486 nearby galaxies. A similar conclusion was reached (Hunt, Malkan 1999) using 891 galaxies in an extended  $12\ \mu\text{m}$  sample (Rush et al. 1993). We should note that their conclusion was based on an optical morphology classification which could be severely affected by dust extinction (e.g., Scoville et al. 1988; Thronson et al. 1989). Near-infrared (NIR) photometric surveys have also suggested that a significant fraction of the Seyfert galaxies show no evidence for the presence of barred potentials (McLeod, Rieke 1995; Mulchaey, Regan 1997), although Seyfert host galaxies seem to be barred more often than non-active galaxies (Knapen et al. 2000; Laine et al. 2002). High angular resolution snapshot surveys using HST NICMOS also failed to find any signature of a strong bar for many of Seyfert galaxies (Regan, Mulchaey 1999; Martini, Pogge 1999; but see Laine et al. 2002). Given the absence of bars, then, what kind of physical processes can drive the ISM into the nuclear region?

In order to investigate the distributions and kinematics of the ISM in non-barred Seyfert galaxies, we carried out high-resolution CO( $J = 1-0$ ) observations of the type-1.5 Seyfert galaxy NGC 5033 (Ho et al. 1997a, 1997b). NIR broad-band photometry was also performed to determine the underlying potential from the stellar surface density, and also to see the distribution of ISM via NIR color. NGC 5033 is classified as non-barred in both the Third Reference Catalogue of Bright Galaxies (RC3; de Vaucouleurs et al. 1991) and A Revised Shapley-Ames Catalog of Bright Galaxies (RSA; Sandage, Tammann 1987). The distribution and kinematics of atomic gas in NGC 5033 have been investigated, and a warping of the galactic plane at larger radii ( $r >$  a few kpc) is reported (e.g., Bosma 1981; Wevers et al. 1986; Thean et al. 1997), but there is little evidence for a bar (Thean et al. 1997). NGC 5033 is therefore a unique target to investigate the distribution and kinematics of ISM in non-barred Seyfert hosts. This galaxy is also suitable for a detailed study of the structure because of its proximity ( $D = 18.7$  Mpc; Tully 1988) and large apparent size ( $10'.7 \times 5'.0$ ; de Vaucouleurs et al. 1991). The basic properties of NGC 5033 are listed in table 1.

We describe millimeter and NIR observations in section 2, and present new results on CO and NIR emission in section 3. In section 4, we show that the molecular gas distribution and kinematics in the central a few kpc region of NGC 5033 are governed by a *small* nuclear bar. Gravitational instabilities of the molecular gas in the center of NGC 5033 are also discussed, implying the absence of strong nuclear star formation in the center of the type-1.5 Seyfert galaxy NGC 5033. We summarize our conclusions in section 5.

## 2. Observations and Data Reduction

### 2.1. CO(1-0) Data with the NMA

The central region of NGC 5033 was observed in the  $J=1-0$  line of CO with the Nobeyama Millimeter Array (NMA). The observations were made during two separated runs, from 1993 December to 1994 April for the C and D configurations, and in 1996 January for the AB configuration. Due to the limitation of the minimum projected baseline length (10 m), extended structures larger than about  $50''$  in each channel map were not sampled in the observations. The front-ends were tunerless SIS receivers, whose receiver temperature was about 40 K in the double side band, and the system noise temperatures (in single side band) were 400 – 800 K during the observations. A digital spectro-correlator FX was configured to cover 320 MHz with 1024 channels per baseline. A side-band separation was achieved by  $90^\circ$  phase switching. We observed a continuum source, 1308+326, every 30 minutes to monitor the temporal variations of the instrumental complex gain. The passband across 1024 channels was calibrated through observations of 3C 273. The flux density of 1308+326 was determined from comparisons with planets of known brightness temperatures. The uncertainty in the absolute flux scale is estimated to be  $\sim \pm 20\%$ . The raw data were calibrated and edited using the package UVPROC-II developed at NRO (Tsutsumi et al. 1997), and then Fourier transformed with natural weighting using the AIPS task MX. A conventional CLEAN method was applied to deconvolve the synthesized beam pattern. The CLEAN beam was  $3''.9 \times 3''.6$  (position angle  $P.A. = 6^\circ$ ). We made  $19.55\ \text{km s}^{-1}$  width CO channel maps at an interval of  $9.78\ \text{km s}^{-1}$ . The typical rms noise level of each channel map is  $30\ \text{mJy beam}^{-1}$ , or  $200\ \text{mK}$  in brightness temperature scale,  $T_b$ . The parameters of the NMA observations are summarized in table 2.

### 2.2. J and K' Band Images with the OASIS

$J$  ( $1.25\ \mu\text{m}$ ) and  $K'$  band ( $2.15\ \mu\text{m}$ ) images of NGC 5033 were obtained with the  $256 \times 256$  element HgCdTe infrared camera OASIS (Yamashita et al. 1995) at the Cassegrain focus of the 188 cm reflector at the Okayama Astrophysical Observatory, on 1996 December 22 and 23. The pixel size of the camera,  $40\ \mu\text{m}$ , corresponds to  $0''.96$  at the focal plane of the F/4.5 camera, providing a field of view of  $4'.1 \times 4'.1$ . In order to avoid saturation due to the bright Seyfert nucleus, each frame was taken with short exposure times (20 s for  $J$  and 5 s for  $K'$ ). The net exposure times were 480 s for the  $J$  band and 400 s for the  $K'$  band, respectively.

Data reduction was made using the NOAO IRAF package. A dark frame was subtracted from each sky frame, and then images were divided by a dome-flat frame. After the flattening, sky-subtracted object images were aligned with respect to the stars in the field and combined. Bad pixels were clipped during the combining. For the absolute flux calibration, HD 105601, which is listed at the UKIRT standard star catalogue, was observed during the same nights. Atmospheric extinction corrections were made, whereas no correction for Galactic extinction was applied. We estimate

an uncertainty of a few % in the magnitudes, mainly due to sky subtraction errors. The resultant spatial resolutions estimated from the profiles of stars in the field were  $1''.7$  for the  $K'$  band and  $3''.2$  for the  $J$  band images, respectively.

### 3. Results

#### 3.1. CO(1–0)

##### 3.1.1. Channel maps

Figure 1 shows CO channel maps from the central  $45'' \times 75''$  region ( $4.1 \text{ kpc} \times 6.8 \text{ kpc}$ ) of NGC 5033. We detected significant ( $> 3\sigma$ ) CO emission in 49 adjacent channels with a velocity range of  $V_{\text{LSR}} = 651.5\text{--}1119.4 \text{ km s}^{-1}$ . This velocity width (full width of zero intensity) of  $479 \text{ km s}^{-1}$  is almost the same as that of the single-dish CO(1–0) profiles (e.g., Heckman et al. 1989; Young et al. 1995; Braine, Combes 1993; Nishiyama, Nakai 2001). In order to estimate the missing flux of our aperture synthesis observations, we compared our data with the existing single-dish observations. This galaxy has been observed repeatedly in the CO(1–0) line with various single-dish telescopes (Stark et al. 1987; Heckman et al. 1989; Braine et al. 1993; Young et al. 1995; Elfhag et al. 1996; Maiolino et al. 1997; Papadopoulos, Seaquist 1998; Vila-Vilaró et al. 1998; Curran et al. 2000; Nishiyama, Nakai 2001). Here, we convolved our data cube to a  $45''$  beam and compared the NMA flux with the FCRAO 14 m observations. The CO flux at the same position as the FCRAO observations [ $\alpha$  (B1950) =  $13^{\text{h}}11^{\text{m}}09^{\text{s}}.7$ ,  $\delta$  (B1950) =  $+36^{\circ}51'30''$ ], is  $325 \pm 8 \text{ Jy beam}^{-1} \text{ km s}^{-1}$ , whereas the FCRAO flux is  $7.2 \pm 0.77 \text{ K km s}^{-1}$  in  $\int T_{\text{a}}^*(v)dv$  or  $302 \pm 32 \text{ Jy beam}^{-1} \text{ km s}^{-1}$  using a sensitivity factor of  $42 \text{ Jy K}^{-1}$  for the  $T_{\text{a}}^*$  scale. (Young et al. 1995). Considering the uncertainties in the absolute flux scale ( $\sim \pm 20\%$ ), most of the single-dish flux seems to be recovered by our observations, and we can safely discuss the distribution and kinematics of the molecular gas below.

##### 3.1.2. CO distribution

A velocity-integrated intensity map of the CO emission is shown in figure 2b, with an optical image of NGC 5033 (figure 2a) from the Digitized Sky Survey. This CO image was obtained from the 0-th moment of the CO data cube with the AIPS task MOMNT. To minimize the contribution from noise, we computed a moment map with a clip level of  $2\sigma$  in each channel map.

The most outstanding feature seen in the integrated intensity map of CO, figure 2b, is two strong CO peaks, which appear to straddle the nucleus. These two CO peaks lie along the major axis of the galaxy ( $P.A. = -8^{\circ}$ ), and are separated by  $\sim 3''$  ( $270 \text{ pc}$ ) from the nucleus. We also find offset ridges of the CO emission, emanating from the two CO peaks, along a  $P.A.$  of about  $-60^{\circ}$ .

It is evident that there is an extended and patchy disk-like structure over the field of view. The outer boundary of the CO emission is almost elliptical, with an axial ratio of about 0.4. This axial ratio can be explained as a disk with an intrinsically circular boundary, at an inclination angle of  $\sim 66^{\circ}$ . This inclination angle of the molecular disk agrees with that of the whole galaxy (table 1; Thean et al. 1997). The radius of the disk-like structure is about  $30'' = 2.7 \text{ kpc}$ . This size is mostly consistent with a  $\sim 7''$  resolution CO map obtained from BIMA observations (Wong, Blitz 2002). A careful inspection of the CO map suggests that some of the CO patches on the “disk” are a part of continuous structures, such as a ring and a spiral arm. The ring and spiral-arm like structures are particularly remarkable in the southern part of the map, as traced by the solid lines in figure 3. These overall CO structure agree well with recent OVRO millimeter array observations (Baker 1999).

Figure 4 shows the CO spectra from the central  $21'' \times 21''$  region of NGC 5033. The CO spectra near the two central peaks are characterized by broad line widths ( $\geq 200 \text{ km s}^{-1}$  in FWHM) and double or multiple peaked profiles, while the CO spectra in the disk region show single Gaussian-shaped profiles and narrow widths ( $\sim 50 \text{ km s}^{-1}$  in FWHM).

##### 3.1.3. Molecular gas mass and surface density

The mass of the molecular gas is estimated from the CO intensity, using a  $N_{\text{H}_2}/I_{\text{CO}}$  conversion factor,  $X_{\text{CO}}$ . Here, we adopted a Galactic  $X_{\text{CO}}$  value of  $1.8 \times 10^{20} \text{ cm}^{-2} (\text{K km s}^{-1})^{-1}$  (Dame et al. 2001).

The surface mass density of molecular hydrogen on the galaxy plane is calculated as

$$\Sigma_{\text{H}_2} = 2.89 \times \cos(i) \cdot \left( \frac{I_{\text{CO}}}{\text{K km s}^{-1}} \right) \left[ \frac{X_{\text{CO}}}{1.8 \times 10^{20} \text{ cm}^{-2} (\text{K km s}^{-1})^{-1}} \right] M_{\odot} \text{ pc}^{-2}, \quad (1)$$

where  $I_{\text{CO}}$  is the CO intensity, and  $i$  is the inclination of the galaxy ( $i = 68^{\circ}$  for NGC 5033). For our CO observations, the  $1\sigma$  level of the CO integrated intensity map,  $2.0 \text{ Jy beam}^{-1} \text{ km s}^{-1}$  or  $13 \text{ K km s}^{-1}$  in  $T_{\text{b}}$ , corresponds to a face-on molecular gas surface density of  $\Sigma_{\text{gas}} = 23 M_{\odot} \text{ pc}^{-2}$  (or a  $\text{H}_2$  column density of  $2.4 \times 10^{21} \text{ cm}^{-2}$ ), and the CO peak (about  $14\sigma$ ) is  $320 M_{\odot} \text{ pc}^{-2}$ , including He and heavier element masses, as  $\Sigma_{\text{gas}} = 1.36 \cdot \Sigma_{\text{H}_2}$ . Note that the gas surface densities don't depend on the adopted distance to the galaxy. The molecular gas density derived here should be compared with the atomic gas surface density; Thean et al. (1997) detected a *peak* HI column density of  $6.5 \times 10^{21} \text{ atoms cm}^{-2}$  ( $22''.7 \times 18''.5$  beam) or a *peak* face-on HI surface density,  $\Sigma_{\text{H}}$ , of  $18 M_{\odot} \text{ pc}^{-2}$ , which is below the

lowest contour in figure 2b and 3 (face-on  $\text{H}_2$  surface density  $\Sigma_{\text{H}_2}$  of  $25 M_{\odot} \text{pc}^{-2}$ ). Although the  $\Sigma_{\text{H}}$  is an averaged value over a much larger area ( $22.''7 \times 18.''5$ ) than our  $\Sigma_{\text{H}_2}$  data ( $3.''9 \times 3.''6$ ), we may conclude that molecular gas dominates the ISM in the central region of NGC 5033.

The molecular gas mass is then computed by multiplying the surface density of the gas by area. Converting a unit of CO intensity from  $\text{K km s}^{-1}$  to  $\text{Jy km s}^{-1}$  per  $\text{arcsec}^2$ , we obtain

$$M(\text{H}_2) = 7.0 \times 10^3 \left( \frac{S_{\text{CO}}}{\text{Jy km s}^{-1}} \right) \left( \frac{D}{\text{Mpc}} \right)^2 \left[ \frac{X_{\text{CO}}}{1.8 \times 10^{20} \text{ cm}^{-2} (\text{K km s}^{-1})^{-1}} \right] M_{\odot}, \quad (2)$$

where  $S_{\text{CO}}$  is the CO flux density, and  $D$  is the distance. The observed CO flux within the central  $r < 30''$  region is  $430 \text{ Jy km s}^{-1}$ , which corresponds to a total molecular gas mass of  $M_{\text{gas}} = 1.4 \times 10^9 M_{\odot}$ , including He and heavier elements ( $M_{\text{gas}} = 1.36 \cdot M_{\text{H}_2}$ ).

### 3.1.4. Radial distribution of molecular gas

Figure 5 shows the radial distribution of the molecular gas surface density in NGC 5033. The integrated intensity of CO in figure 2b was azimuthally averaged over successive annuli with  $1'' = 90.7 \text{ pc}$  width using the AIPS task IRING, and was used to calculate the face-on molecular gas surface density by adopting the above formula. The maximum gas surface density is located at a radius of  $\sim 400 \text{ pc}$  ( $\sim 4.''4$ ), not at the center. A second increase in the gas surface density is also evident at  $r \sim 1.3 \text{ kpc}$  ( $\sim 14''$ ), which corresponds to the radius of the ‘‘partial ring’’ denoted in figure 3.

### 3.1.5. Velocity field

Figure 2c shows an intensity-weighted isovelocity contour map of the CO emission. This map was made by computing the first moment of the CO data cube, as  $\langle v \rangle = \Sigma_i v_i S_i / \Sigma_i S_i$ . It is evident that circular motion dominates the kinematics in the central a few kpc region of NGC 5033 because a systematic change in the positions of the emission as a function of velocity with the overall symmetry can be seen, suggesting an ordered circular motion. However, as seen in the channel maps, this CO velocity field also reveals a ‘‘Z-shape’’ twist of isovelocity contours near the systemic velocity, which is a signature of non-circular motions. It is also clear that the isovelocity contours near the center tend to align with the position angle of the CO ridges ( $P.A. \sim -60^\circ$ ), rather than the kinematical minor axis ( $P.A. \sim -98^\circ$ ). In a pure circular rotation case, the isovelocity contours near the systemic velocity should be straight lines perpendicular to the kinematical major axis (i.e., aligned to the minor axis). This deviation is also evident in the velocity channel maps of  $V_{\text{LSR}} = 866 - 895 \text{ km s}^{-1}$  in figure 1.

We determined the kinematical parameters of the gas disk (dynamical center, position angle of the major axis, inclination angle, and systemic velocity) by a least-squares fitting of the intensity-weighted isovelocity field as a circular rotation. We used the GAL package in AIPS for this analysis. The derived parameters are listed in table 3. These results agree with values determined from the  $\sim 20''$  resolution HI observations (Thean et al. 1997). It should be noted that the observed CO velocity field contains local deviations from circular rotation, as described above; however, and the kinematic parameters derived here can be affected by the non-circular motions. Hence,, we adopted those determined by Thean et al. (1997) in the following analysis.

### 3.1.6. P–V diagram and rotation curve

A position–velocity diagram (P–V diagram) along the major axis ( $P.A. = -8^\circ$ ) of NGC 5033 is displayed in figure 6.

We determined the circular rotation curve of the inner part of NGC 5033 from our CO data by averaging the intensity-weighted mean velocities (figure 2c) within a  $\pm 5^\circ$  area along the major axis of the galaxy, using the GAL package in AIPS. The resultant rotation curve is shown in figure 7.

The rotation velocities at the flat part are  $\sim 220 \text{ km s}^{-1}$  on the plane of the disk (adopting  $i = 68^\circ$ ). This agrees well with the  $\sim 20''$  resolution HI observations (Thean et al. 1997) and  $16''$  resolution CO observations (Sofue 1997; Nishiyama et al. 2001).

Near the center ( $r < 10''$ ), this diagram shows a gradual rise of the rotation velocity. Smearing of the observing beam is a possible cause of this *gradual* rise, and the true rotation velocity could be larger there. The CO spectra near the center shows very broad and multiple velocity components (figure 4), and a simple moment analysis could fail to trace the true rotation velocities in this case.

In fact, the P–V diagram in figure 6 shows a very steep rise of the rotation velocities near the center if we trace the terminal velocities as the true rotation velocities; it reaches a constant (flat rotation) at  $r \sim 2''$ . Given our finite spatial resolution, the turnover radius of the rotation curve ( $r \sim 2''$ ) could be an upper limit.

Another possibility of a *gradual* rise of the circular rotation velocity is a bar; non-circular motion associated with the presence of a bar may be the cause of a steeper P–V diagram than the actual rotation curve (Bureau, Athanassoula 1999; Athanassoula, Bureau 1999).



It should be noted that the velocity field contains significant non-circular motions, and the derived values must be treated as an averaged rotation curve (e.g., Sakamoto et al. 1999a), possibly with significant local deviations.

From these considerations, we here assume a constant rotation velocity of  $220 \text{ km s}^{-1}$  for  $r > 2''$ , and a rigid-body rotation of  $\Omega = 1.2 \text{ km s}^{-1} \text{ pc}^{-1}$  for  $r < 2''$ . This rotation curve is indicated as the dashed line in figure 7, and is applied to resonance identifications in the following discussion (subsection 4.2).

Note that Baker (1999) reported that there is a kinematically decoupled gas component just around the center of NGC 5033 (i.e., between the two CO peaks in figure 2b) based on a P–V diagram of the OVRO interferometer CO(2–1) data; however, the CO(1–0) emission in our map seems to be too weak to identify such features.

### 3.1.7. Velocity dispersion

Figure 8 shows the intensity-weighted CO velocity dispersion along the line of sight, as derived from the second moment of the CO data cube,  $\sigma_v = \Sigma_i (v_i - \langle v \rangle)^2 S_i / \Sigma_i S_i$ . It should be noted that this map contains both the intrinsic velocity dispersion of the gas and the gradient of the rotation velocity in the observing beam; the very large velocity dispersion area along the minor axis of the galaxy represents the steep rise of the rotation curve in the central region of the galaxy. Near the center of the galaxy, it is evident that the second moment values at the two central CO peaks are quite large ( $> 45 \text{ km s}^{-1}$ ) compared with other regions. The CO line profiles in this area appear to deviate from a simple Gaussian shape, and are perhaps multiple-peaked, as can be seen in figure 4. Therefore, the second moment values near the central CO peaks should not be treated as a velocity dispersion of gas, yet complex gas kinematics near the two central CO peaks is suggested.

## 3.2. NIR Images

### 3.2.1. Isophotos

$J$  and  $K'$  band images obtained with the OASIS observations are presented in figure 9. The surface brightness at the outer boundary is about  $19 \text{ mag arcsec}^{-1}$  in the  $K'$  band, and  $21 \text{ mag arcsec}^{-1}$  in the  $J$  band, respectively. We also show contour maps of the  $K'$  band in the central  $40'' \times 40''$  region in figure 10. The overall  $K'$  band structures agree with the previous NIR observations (McLeod, Rieke 1995; Peletier et al. 1999).

In order to quantify the incidence of a bar, we have fitted ellipses to isophotos of each band using the routine ELLIPSE in the STSDAS package within IRAF. Radial profiles of the surface brightness, ellipticity, and position angle derived from the ellipse fits of the  $K'$  band data are given in figure 11. Because of the better seeing size in  $K'$  than that of the  $J$  band, the ellipse fitting near the nucleus is more reliable in the  $K'$  band.

We find that the position angle abruptly changes from  $\sim -8^\circ$  (i.e., the same as the position angle of galactic disk major axis) to  $\sim -23^\circ$  at a semimajor axis of  $\sim 8''$  or 730 pc. This can also be seen in the contour map in figure 10, and may suggest the existence of an oval distortion. It is difficult to conclude the presence of a bar here, however. Generally, the criteria for the identification of bars are (i) the ellipticity increases as a function of the radius to a maximum, and then decreases to reveal the inclination of the disk, and (ii) the position angle is constant over the radii where the ellipticity is rising (McLeod, Rieke 1995; Mulchaey et al. 1997), but the highly inclined disk of NGC 5033 prevents us from a reliable identification of the bars. Moreover, we find that the existence of the molecular spiral arms could also influence the isophotos, even in the  $K'$  band.

If the observed NIR features are 2-dimensional, we can deproject the isophotal contours by expanding figure 10 along the minor axis by a factor of  $(\cos i)^{-1}$ ; we then see the elongated distribution of the  $K'$  emission at a semi-major length of  $\sim 15''$ . However, it is likely that the true distribution of low-mass stars, which dominate the  $K'$  emission observed here, is 3-dimensional, and hence the “deprojection” of the contour maps gives an upper limit of the oval structures in the  $K'$ -band emission.

### 3.2.2. $J - K'$ color

The  $K'$ -band image was convolved to the same resolution as the  $J$ -band data, and a  $J - K'$  color map was produced. Figure 12 shows the  $J - K'$  color map and a comparison with the integrated CO intensity image. The CO image was aligned to NIR maps postulating the NIR continuum peak as the position of the Seyfert nucleus.

A circumnuclear ring with a radius of  $\sim 1.3 \text{ kpc}$  and two spiral arms are clearly seen in the  $J - K'$  color. These spirals are also clearly confirmed by the high angular resolution NIR colors (Peletier et al. 1999). We see that the ring and the two spiral arms in the  $J - K'$  color map agree well qualitatively with the CO distribution. We can trace the successive CO peaks along the ring and two spirals seen in the  $J - K'$  map. The two spirals seen in the  $J - K'$  map terminate at a radius of  $\sim 30''$  as well as the CO map. Thus, the abrupt cut-off of the CO emission seen in figure 2b means that most of the ISM, including HI gas, is really concentrated within this radius. This is supported by a CO mapping over the entire disk (Nishiyama, Nakai 2001; Curran et al. 2001; Wong, Blitz 2002) and an  $850 \mu\text{m}$  dust continuum map (Doi 2002, private communication).

Good correlations between CO maps and NIR color maps have been reported in other spiral galaxies (e.g., Sakamoto et al. 1995; Hurt et al. 1996; Regan 2000). The correspondence between CO and  $J - K'$  color is particularly significant in the western side of the galaxy. This could mean that the western part of the galaxy is the near side; because the

ISM would be distributed on a thin disk-like plane, in contrast to stars, more stars on the near side are reddened than those on the far side. This configuration indicates that the spiral arms seen in optical and CO images are trailing.

On the other hand, we see a significant discrepancy between the NIR color index and the CO distribution within the central  $r \leq 5''$  region; the color map shows a single peak at the Seyfert nucleus, whereas there exist two CO peaks apart from the nucleus. It could be likely that the NIR color near the active nucleus no longer reflects the dust extinction (and therefore the distribution of the ISM), as in the case of the nucleus in NGC 1068 (Hurt et al. 1996). In fact, HST observations of NGC 5033 at 1.6  $\mu\text{m}$  band show an unresolved source in the center of NGC 5033. It must be from the non-stellar activity, because its flux correlates with the hard X-ray luminosity (Quillen et al. 2001). The  $J - K'$  index toward the nucleus is 1.21 mag in NGC 5033, which is a redder color. Similar  $J - K'$  color indices toward Seyfert nuclei can be found in the literature (e.g., Forbes et al. 1992; Hunt, Giovanardi 1992; Alonso-Herrero et al. 1996, 1998; Peletier et al. 1999).

#### 4. Discussion

Our high-resolution CO and NIR observations reveal a non-axisymmetric molecular gas distribution and perturbed gas kinematics in the central  $\sim$  kpc region of NGC 5033. The observed morphological features are: (i) two strong CO peaks straddling the nucleus, separated by  $\sim 3''$  or 270 pc from the nucleus, (ii) a molecular ring with a radius of  $\sim 14''$  or 1.3 kpc, (iii) offset molecular ridges connecting the two CO peaks and the molecular ring, and (iv) two-armed molecular spirals that terminate abruptly at a radius of  $\sim 30''$  or 2.7 kpc. We also find kinematical features: (v) double peaked and wide CO line profiles near the two CO peaks, and (vi) a twist of the isovelocity contours near the systemic velocity, which tend to align with the position angle of the CO ridges.

In this section, we show that all of the observed molecular gas distribution and kinematics can be understood as a response to a *small* nuclear bar. We also discuss the gravitational instabilities of molecular gas in the center of NGC 5033 in order to show that no starburst coexists in the low-luminosity type-1.5 Seyfert nucleus of NGC 5033.

##### 4.1. Signature of a Nuclear Bar in NGC 5033

The observed features listed above are reminiscent of those in the central regions of barred spiral galaxies; first, the two conspicuous CO peaks which appear to straddle the nucleus of the NGC 5033 quite resemble the ‘‘CO twin peaks’’ widely observed in the central regions of barred galaxies (e.g., Kenney et al. 1992; Kenney 1996). Second, the elongations of CO emission from two CO peaks mimic the dust-lane morphology of barred galaxies (e.g., Athanassoula 1992). Offset ridge structures of CO emission along the leading sides of a bar are often observed in the central regions of barred galaxies, such as IC 342 (Ishizuki et al. 1990), NGC 1530 (Reynaud, Downes 1998; Regan et al. 1999), and NGC 3504 (Kuno et al. 2000). These morphological similarities of the CO distribution tempt us to consider the existence of a bar at a position angle of  $-50^\circ \pm -10^\circ$ , because the twin peaks seen in barred galaxies are usually oriented perpendicular to the stellar bars, and because CO ridges should be located at the leading sides of the bars. The observed velocity field, where isovelocity contours deviate from the circular motion and tend to align with the position angle of the CO ridges, is also consistent with the presence of a bar. This is because models of the gas dynamics in a barred potential predict that the largest velocity gradient should be seen across the bar (e.g., Robert et al. 1979); in fact, such features have been observed in the central regions of galaxies with bars.

In addition to these, the apparent disagreement between the P–V diagram and the circular rotation velocities from a moment map seen in figure 7 could also be a suggestive of a bar. As mentioned in subsection 3.1.6, a steeper P–V than the rotation curve can occur due to a bar (Bureau, Athanassoula 1999; Athanassoula, Bureau 1999).

##### 4.2. Nuclear Bar and Dynamical Resonances

In order to check whether an orbit resonance theory can explain the observed gas distribution, we examined the angular velocities of the molecular gas. The inner Lindblad resonances (ILRs) will exist wherever  $\Omega(r) - \kappa(r)/2 = \Omega_{\text{bar}}$  at some location within the corotation, where  $\Omega(r)$  is the rotation frequency at a radius of  $r$  [i.e.,  $= v(r)/r$ ],  $\Omega_{\text{bar}}$  is the rotation frequency of the bar (the pattern speed of the bar, and is constant with radius), and  $\kappa(r)$  is the epicyclic frequency. For a higher order resonance, the ultra harmonic resonance (UHR; 4:1 resonance) can also occur, where  $\Omega(r) - \kappa(r)/4 = \Omega_{\text{bar}}$ .

We think that there are two possible loci of the corotation resonance [CR; it occurs where  $\Omega(r) = \Omega_{\text{bar}}$ ] from the observed CO distribution: one is to assume that (i) a cut-off of the molecular gas distribution corresponds to a possible corotation radius, giving a possible CR radius  $R_{\text{CR}} \sim 30''$  or 2.7 kpc, and the other is (ii) to assume the CR lies near  $R_{\text{CR}} \sim 23''$  or 2.1 kpc, where a local dip of CO is seen in the radial distribution of the molecular gas (figure 5). These are because barred potentials sweep gas clouds inwards from the corotation up to ILRs; also because the gas outside the corotation tends to accumulate near the outer Lindblad resonance (OLR), the ISM would be depopulated in the corotation resonance. This scenario has been successfully applied to several galaxies, such as NGC 891 (García-Burillo, Guélin 1995) and NGC 253 (Houghton et al. 1997). These assumptions immediately yield possible bar pattern-speeds of  $\Omega_{\text{bar}} \sim 85 \text{ km s}^{-1} \text{ kpc}^{-1}$  for the first case (i) and  $\Omega_{\text{bar}} \sim 105 \text{ km s}^{-1} \text{ kpc}^{-1}$  for the latter case (ii), respectively,

adopting the rotation curve discussed in subsection 3.1.6 (also see figure 6).

Figure 13 shows the angular velocities as a function of the galactocentric radius, i.e.,  $\Omega(r) = v(r)/r$ ,  $\Omega(r) \pm \kappa(r)/2$ , and  $\Omega(r) - \kappa(r)/4$ , where  $\kappa(r) = \{2[v(r)/r] \cdot [v(r)/r + dv(r)/dr]\}^{0.5}$ , as well as the proposed range of the bar pattern speeds,  $\Omega_{\text{bar}}$ . This resonance analysis means that the two observed CO peaks and the elongated CO ridges lie between the inner ILR (IILR) and outer ILR (OILR). This situation is widely observed in the central regions of barred galaxies (e.g., Kenney et al. 1992; Telesco et al. 1993; Kenney 1996; Downes et al. 1996; Kohno et al. 1999a), although it must be treated with caution, because non-circular motions near the center of barred galaxies can severely affect the estimation of ILR radii (Sakamoto et al. 1999a). These CO peaks are considered to be orbit crowding zones where different families of gas streams,  $x_1$  and  $x_2$ , would be crossing. This would result in shocks along the orbit crowding region, as suggested by theory (e.g., Athanassoula 1992). In fact, very large velocity dispersion and/or complex CO spectra with two or more peaks have been observed near the “twin peaks” of barred galaxies (Kenney 1996; Kohno et al. 1999a; Sorai et al. 2000; Koda et al. 2002), adding another bit of evidence for a bar-driven gas motion. Figure 13 also shows that the 1.3 kpc ring feature may correspond to the UHR if  $\Omega_{\text{bar}} \sim 105 \text{ km s}^{-1} \text{ kpc}^{-1}$  (i.e., the assumption (ii)). Nuclear rings possibly explained by UHR are observed in barred spiral galaxies, such as NGC 253 (Sorai et al. 2000) and NGC 5005 (Sakamoto et al. 2000); we therefore suggest that the larger  $\Omega_{\text{bar}}$  (i.e.,  $\sim 105 \text{ km s}^{-1} \text{ kpc}^{-1}$ ) may be more plausible. Considering the uncertainties of the rotation velocities, we conclude here that  $R_{\text{CR}}$  is in the range of about 2.1 – 2.7 kpc.

Given the  $R_{\text{CR}} = 2.1 - 2.7 \text{ kpc}$ , this would also impose an upper limit on the bar length. In early type galaxies, it is now widely accepted that the corotation radius lies near to the bar end; that is,  $R_{\text{CR}}$  is  $\sim 1.2 \pm 0.2 R_{\text{bar}}$  (Athanassoula 1992; Elmegreen 1996). On the other hand, a numerical simulation by Combes and Elmegreen (1993) suggested that bars in late-type galaxies may have their corotation radii well outside the bar ends; possibly,  $R_{\text{CR}}$  is  $\sim 2 R_{\text{bar}}$  (see also Kuno et al. 2000). Consequently, the possible bar radius (semi-major radius) in NGC 5033 would be in the range of about 0.5 – 1.2  $R_{\text{CR}}$ , i.e., 1.1 – 3.2 kpc, and probably near 0.5  $R_{\text{CR}}$  or 1.1 – 1.4 kpc, as in the case of the bars in other late-type spirals, such as M 100 (García-Burillo et al. 1994; Sempere et al. 1995; Elmegreen et al. 1992).

The possible bar radius of  $\sim 1.1 - 1.4 \text{ kpc}$  is also implied from the observed radial distribution of CO emission; recent CO observations of barred galaxies demonstrate the existence of a “secondary peak” of the ISM near the bar-ends (Kenney, Load 1991; Nakai 1992; Downes et al. 1996; Nishiyama et al. 2001), and the second enhancement of CO emission at a radius of  $\sim 1.3 \text{ kpc}$  seen in the CO radial distribution of figure 4 may suggest that a plausible bar radius in NGC 5033 would indeed be  $\sim 1.1 - 1.4 \text{ kpc}$ .

We should note that NGC 5033 has several rings in the outer disk region ( $r >$  a few arcmin), as can be seen in the HI maps (Thean et al. 1997). These outer rings seem to be difficult to explain by only the small nuclear bar proposed here, because the OLR of the nuclear bar would be located at about  $r \sim 3.7 \text{ kpc}$  or  $\sim 40''$ , which is much more inward than the outer HI rings. However, it is possible to understand the whole structure if NGC 5033 has multiple bars; S. Ishizuki (2002, private communication) proposed that there are three bars in the disk of NGC 5033 based on the deprojected HI map (Thean et al. 1997), assuming that the ILR radii of the outer bars correspond to the corotation radii of the inner bars (Friedli, Martinet 1993).

In summary, both the distribution and kinematics of the molecular gas in the central region of NGC 5033 can be well understood as the response to a bar. We propose that a small nuclear bar lies along a position angle of  $-50^\circ \pm -10^\circ$  and a possible semi-major radius of  $R_{\text{bar}} \sim 1.1 - 1.4 \text{ kpc}$  ( $12'' - 15''$ ). The pattern speed of the nuclear bar is estimated to be  $85 - 105 \text{ km s}^{-1} \text{ pc}^{-1}$ . Figure 14 displays our proposed interpretation of the gas distribution in the center of the “non-barred” Seyfert galaxy NGC 5033. This small nuclear bar would sweep the molecular gas inside the corotation radius and channel it into the central region of the galaxy.

Our results also demonstrate that high-resolution CO imaging-spectroscopy is useful to search for a bar even in highly inclined systems where isophoto ellipse fitting techniques are not applicable.

#### 4.3. Role of a Nuclear Bar

The fact that  $\sim 20''$  resolution HI observations show little evidence for a bar in NGC 5033 (Thean et al. 1997) would suggest that a large-scale nonaxisymmetry of underlying potential is not required for Seyfert activity, and that high-resolution observations of the ISM are crucial for studying the fueling mechanism of Seyfert galaxies. As pointed out by McLeod and Rieke (1995), the critical elements of the fuel supply need not be visible on the *large scale* in the host galaxy. In fact, the possible bar length in NGC 5033 is quite small; the semi-major radius of  $\sim 1.1 - 1.4 \text{ kpc}$  corresponds to only  $\sim 0.02 \times D_{25}$ . We should also note that a very weak bar can play a significant role on the ISM. Numerical simulations have predicted that the molecular gas distribution and kinematics severely affected even in a potential with a very weak asymmetry, a few % or less in density (Wada, Habe 1992; Jungwiert, Palous 1996), which might not be easy to detect, even in the NIR bands. Hence, it seems that the apparent lack of a clear and strong bar/oval structure in the stellar surface density traced with NIR continuum emission does not immediately mean that the ISM in such galaxies is not driven into the central regions by a bar.

Nevertheless, it appears to be clear that the presence of a small-scale bar is *not a sufficient* condition for Seyfert activity, though it could be a necessary condition. As described in the previous sections, bar-driven gas structures,

such as the “twin-peaks” seen in NGC 5033, are widely observed in many barred spiral galaxies, but not every barred galaxy hosts an active nucleus. Additional mechanisms, such as self-gravity of ISM (e.g., Wada, Habe 1992; Heller, Shlosman 1994) or a “nuclear ILR” induced by the central super massive black holes (Fukuda et al. 1998, 2000), would be necessary to drive ISM into the central engine.

It should also be noteworthy that a very small amount of gas is sufficient to sustain low-level Seyfert activities. The required mass accretion rates,  $\dot{M}$ , in order to feed a given luminosity,  $L_{\text{bol}}$ , are expected to be

$$\dot{M} = \frac{L_{\text{bol}}}{\eta c^2} = 2.0 \times 10^{-2} \left( \frac{\eta}{0.1} \right)^{-1} \left( \frac{L_{\text{bol}}}{10^{44} \text{ erg s}^{-1}} \right) M_{\odot} \text{yr}^{-1}, \quad (3)$$

(Rees 1984) for a typical luminosity of Seyfert galaxies, where  $\eta$  is the accretion efficiency. Because NGC 5033 is a low-luminosity Seyfert ( $L_{2-10\text{keV}} = 2.3 \times 10^{41} \text{ erg s}^{-1}$ , Terashima et al. 1999; see also Koratkar et al. 1995), the required gas mass is only  $\sim 10^5 M_{\odot}$  to feed the monster over a time of  $\sim 10^9 \text{ yr}$ . This may explain why not all Seyfert hosts are barred; a high  $\dot{M}$ , which can be achieved by a bar, is not always required for low-luminosity AGNs (Ho et al. 1997c).

#### 4.4. Star Formation and Self Gravity of Molecular Gas in Seyfert Nuclei

A massive nuclear starburst is often associated with Seyfert galaxies. In particular, a large fraction (about 50%, Storchi-Bergmann et al. 2001) of type-2 Seyfert nuclei are reported to coexist with a nuclear starburst (e.g., Heckman et al. 1997; Maiolino et al. 1998; González Delgado et al. 1998; Cid Fernandes et al. 2001; Imanishi 2002). These nuclear starbursts can be in the dense obscuring torus (e.g., Cid Fernandes, Terlevich 1995), which would play an important role to form a geometrically thick torus via energy feedback from supernovae (Fabian et al. 1998; Wada, Norman 2002).

In order to address the nuclear star formation in the type-1.5 Seyfert galaxy NGC 5033, we examined the gas mass fraction to the dynamical mass,  $M_{\text{gas}}/M_{\text{dyn}}$ , in the center of NGC 5033. In galaxies with nuclear starburst/star formation,  $M_{\text{gas}}/M_{\text{dyn}}$  often exceeds 10% (e.g., Kenney et al. 1993; Sakamoto et al. 1999b). Such a high gas fraction results in the unstable states of molecular gas, and eventually massive star formation occurs there (e.g., Elmegreen 1994). Therefore, the  $M_{\text{gas}}/M_{\text{dyn}}$  values can be a rough diagnostic of starbursts in the centers of galaxies.

The dynamical mass within a given radius  $r$  is calculated as

$$M_{\text{dyn}} = \frac{rv^2(r)}{G} = 2.3 \times 10^5 \left( \frac{r}{\text{kpc}} \right) \left[ \frac{v(r)}{\text{km s}^{-1}} \right]^2 M_{\odot}, \quad (4)$$

where  $v(r)$  is a circular rotation velocity at a galactocentric radius of  $r$ , assuming a spherical mass distribution. The dynamical mass within a radius of  $30''$  or 2.7 kpc, the outer boundary of the CO emission, was then calculated to be  $3.0 \times 10^{10} M_{\odot}$ , and the ratio of dynamical mass to the total molecular gas mass  $M_{\text{gas}}/M_{\text{dyn}}$  is 0.081 within  $r < 2.7$  kpc. The gas mass ratio,  $M_{\text{gas}}/M_{\text{dyn}}$ , remains almost constant over the molecular disk; the  $M_{\text{gas}}/M_{\text{dyn}}$  within  $r < 1.4$  kpc ( $15''$ ), which corresponds to the radius of the molecular ring, is found to be 0.063. It drops to 0.006 in the very center ( $r < 2''$  or 180 pc), however.

This  $M_{\text{gas}}/M_{\text{dyn}}$  of 0.006 is very small compared with that in nuclear starburst galaxies, where the ratio often exceeds 0.1 (e.g., Sakamoto et al. 1999b). We therefore suggest that the molecular gas in the central  $r < 200 \text{ pc}$  region of NGC 5033 may not be self-gravitating, in contrast to the situation in nuclear starburst galaxies. This implies that no nuclear starburst coexists in the center of the type-1.5 Seyfert galaxy NGC 5033, in accord with high-resolution NIR spectroscopic studies (Ivanov et al. 2000; Imanishi 2002), though extended star-forming regions exist in the disk of NGC 5033 (e.g., Clavel et al. 2000; Wang, Blitz 2002). Further analysis of high-resolution molecular gas data in type-1 Seyferts and a comparison with that in type-2s will help in the study of the role of nuclear starbursts in the AGN phenomenon.

The uncertainty of the derived  $M_{\text{gas}}/M_{\text{dyn}}$  values could be large near the center, because the circular rotation velocity adopted here can be affected by the presence of non-circular motions in the central region of NGC 5033. Nevertheless, the  $M_{\text{gas}}/M_{\text{dyn}}$  values in the center of NGC 5033 can be very small because the molecular gas mass near the center of NGC 5033 may be overestimated; the conversion factors in the central regions of galaxies (including the Galactic Center region) tend to be *smaller* than those in the Galactic disk GMCs by a factor of 3 – 10 or more (e.g., Nakai, Kuno 1995; Solomon et al. 1997; Oka et al. 1998; Dahmen et al. 1998; Regan 2000), which would result in a further decreasing of  $M_{\text{gas}}/M_{\text{dyn}}$  in the nucleus of NGC 5033.

## 5. Conclusions

Our high-resolution aperture synthesis CO(1–0) observations and NIR broad-band photometry were performed toward the central region of the “non-barred” Seyfert galaxy NGC 5033. The results of the observations are summarized as follows:



1. Our high-resolution CO images reveal a perturbed distribution of molecular gas in the center of the “non-barred” Seyfert galaxy NGC 5033; we find (i) two strong CO peaks straddling the nucleus, separated by  $\sim 3''$  or 270 pc from the nucleus, (ii) a molecular ring with a radius of  $\sim 14''$  or 1.3 kpc, and (iii) offset molecular ridges connecting the two CO peaks and the molecular ring. These are the characteristic gaseous features that are widely observed in the centers of barred galaxies.
2. We find that broad ( $\geq 200 \text{ km s}^{-1}$  in FWHM) and double-peaked profiles are seen near the two CO peaks, which would support the idea that the two observed CO concentrations are the orbit crowding regions where different families of gas orbits ( $x_1$  and  $x_2$ ) in the bar meet there. The observed velocity field also suggests the presence of a bar in NGC 5033.
3. Outside the ring, we find two armed spiral structures, which abruptly terminate at the radius of  $\sim 30''$  or 2.7 kpc, showing an excellent agreement to the  $J - K'$  color index map. However, in the very center of the active nucleus, the  $J - K'$  color does not reflect the distribution of ISM.
4. Based on the resonance analysis of the molecular gas, we propose that the gas distribution and kinematics in the central a few kpc region of NGC 5033 are governed by a small nuclear bar. The possible bar properties, i.e., the position angle, semi-major radius, and pattern speed, are estimated to be about  $-50^\circ \pm 10^\circ$ ,  $\sim 1.1 - 1.4 \text{ kpc}$  ( $12'' - 15''$ ), and  $\sim 85 - 105 \text{ km s}^{-1} \text{ pc}^{-1}$ , respectively. The parameter of the nuclear bar proposed here can account for all of the observed CO features with consistency.
5. Although we could not confirm the presence of a nuclear bar from NIR photometry due to the high inclination angle of NGC 5033, we did obtain an upper limit of the bar radius,  $\sim 20''$ . This is consistent with the size of the bar deduced from the CO data. These results demonstrate that high-resolution CO imaging-spectroscopy is useful to search for a bar even in highly inclined systems where isophoto fitting techniques are not applicable.
6. The fraction of molecular gas mass to the dynamical mass,  $M_{\text{gas}}/M_{\text{dyn}}$ , is very small ( $\leq 1\%$  within  $r < 2''$  or 180 pc). This would suggest that the molecular gas accumulated in this region is not self-gravitating, in contrast to nuclear starburst/star-forming galaxies, implying no nuclear starburst coexists in the type-1.5 Seyfert galaxy NGC 5033. It should be noted that the  $M_{\text{gas}}/M_{\text{dyn}}$  values near the center could contain large uncertainties due to a strong non-circular motion in the central region of NGC 5033, however.

We would like to thank the referee for helpful comments that improved this paper. We are deeply indebted to the NRO staff for operating the telescopes and continuous efforts to improve the performance of the instruments. We are grateful to A. Mori for his extensive help during the observations at Okayama Astronomy Observatory, S. Okumura and T. Minezaki for their advice and comments on the data reduction and interpretation of our NIR data, and T. Kamazaki for providing us with his useful software packages to make figures in this paper. Nobeyama Radio Observatory (NRO) and Okayama Astrophysical Observatory (OAO) are a branch of the National Astronomical Observatory, an interuniversity research institute, operated by the Ministry of Education, Culture, Sports, Science and Technology.

## References

- Alonso-Herrero, A., Simpson, C., Ward, M. J., & Wilson, A. S. 1998, *ApJ*, 495, 196
- Alonso-Herrero, A., Ward, M. J., & Kotilainen, J. K. 1996, *MNRAS*, 278, 902
- Athanassoula, E. 1992, *MNRAS*, 259, 345
- Athanassoula, E., & Bureau, M. 1999, *ApJ*, 522, 699
- Baker, A. J. 1999, in *The Physics and Chemistry of the Interstellar Medium*, ed. V. Ossenkopf, J. Stutzki, & G. Winnewisser (Herdecke, GCA-Verlag), 30
- Bureau, M., & Athanassoula, E. 1999, *ApJ*, 522, 686
- Bosma, A. 1981, *AJ*, 86, 1791
- Braine, J., Combes, F., Casoli, F., Dupraz, C., Gérin, M., Klein, U., Wielebinsky, R., & Brouillet, N. 1993, *A&AS*, 97, 887
- Cid Fernandes, R., Heckman, T., Schmitt, H., González Delgado, R. M., & Storchi-Bergmann, T. 2001, *ApJ*, 558, 81
- Cid Fernandes, R., Jr., & Terlevich, R. 1995, *MNRAS*, 272, 423
- Clavel, J., Schulz, B., Altieri, B., Barr, P., Claes, P., Heras, A., Leech, K., Metcalfe, L., & Salama, A. 2000, *A&A*, 357, 839
- Combes, F., & Elmegreen, B. G. 1993, *A&A*, 271, 391
- Curran, S. J., Aalto, S., & Booth, R. S. 2000, *A&AS*, 141, 193
- Curran, S. J., Polatidis, A. G., Aalto, S., & Booth, R. S. 2001, *A&A*, 373, 459
- Dahmen, G., Hüttemeister, S., Wilson, T. L., & Mauersberger, R. 1998, *A&A*, 331, 959
- Dame, T. M., Hartmann, D., & Thaddeus, P. 2001, *ApJ*, 547, 792
- de Vaucouleurs, G., de Vaucouleurs, A., Corwin, H. G., Buta, R. J., Paturel, G., & Fouque, P. 1991, *Third Reference Catalogue of Bright Galaxies* (New York, Springer-Verlag)
- Downes, D., Reynaud, D., Solomon, P. M., & Radford, S. J. E. 1996, *ApJ*, 461, 186
- Eckart, A., & Genzel, R. 1996, *Nature*, 383, 415
- Elf Hag, T., Booth, R. S., Høglund, B., Johansson, L. E. B., & Sandqvist, A. 1996, *A&AS*, 115, 439
- Elmegreen, B. 1996, in *Barred Galaxies*, ed. R. Buta, D. A. Crocker, & B. G. Elmegreen (San Francisco, ASP), 197
- Elmegreen, B. G. 1994, *ApJ*, 425, L73
- Elmegreen, B. G., Elmegreen, D. M., & Montenegro, L. 1992, *ApJS*, 79, 37
- Fabian, A. C., Barcons, X., Almaini, O., & Iwasawa, K. 1998, *MNRAS*, 297, L11

- Fukuda, H., Habe, A., & Wada, K. 2000, *ApJ*, 529, 109
- Fukuda, H., Wada, K., & Habe, A. 1998, *MNRAS*, 295, 463
- Forbes, D. A., Ward, M. J., DePoy, D. L., Boisson, C., & Smith, M. S. 1992, *MNRAS*, 254, 509
- Friedli, D., & Martinet, L. 1993, *A&A*, 277, 27
- García-Burillo, S., & Guélin, M. 1995, *A&A*, 299, 657
- García-Burillo, S., Sempere, M. J., & Combes, F. 1994, *A&A*, 287, 419
- González Delgado, R. M., Heckman, T., Leitherer, C., Meurer, G., Krolik, J., Wilson, A. S., Kinney, A., & Koratkar, A. 1998, *ApJ*, 505, 174
- Heckman, T. M., Blitz, L., Wilson, A. S., Armus, L., & Miley, G. K. 1989, *ApJ*, 342, 735
- Heckman, T. M., González Delgado, R., Leitherer, C., Meurer, G. R., Krolik, J., Wilson, A. S., Koratkar, A., & Kinney, A. 1997, *ApJ*, 482, 114
- Helfer, T. T., & Blitz, L. 1995, *ApJ*, 450, 90
- Heller, C. H., & Shlosman, I. 1994, *ApJ*, 424, 84
- Ho, L. C. 1999, in *Observational Evidence for Black Holes in the Universe*, ed. S. K. Chakrabarti (Kluwer, Dordrecht), 157
- Ho, L. C., Filippenko, A. V., & Sargent, W. L. W. 1997a, *ApJS*, 112, 315
- Ho, L. C., Filippenko, A. V., Sargent, W. L. W., & Peng, C. Y. 1997b, *ApJS*, 112, 391
- Ho, L. C., Filippenko, A. V., & Sargent, W. L. W. 1997c, *ApJ*, 487, 591
- Houghton, S., Whiteoak, J. B., Koribalski, B., Booth, R., Wiklind, T., & Wielebinski, W. 1997, *A&A*, 325, 923
- Hunt, L. K., & Giovanardi, C. 1992, *AJ*, 104, 1018
- Hunt, L. K., & Malkan, M. A. 1999, *ApJ*, 516, 660
- Hurt, R. L., Turner, J. L., Levine, D., Merrill, K. M., & Gatley, I. 1996, in *Astronomy with Millimeter and Submillimeter Wave Interferometry*, ed. M. Ishiguro & Wm. J. Welch (San Francisco, ASP), 370
- Imanishi, M. 2002, *ApJ*, 569, 44
- Ishizuki, S., Kawabe, R., Ishiguro, M., Okumura, S. K., Morita, K.-I., Chikada, Y., & Kasuga, T. 1990, *Nature*, 344, 224
- Ivanov, V. D., Rieke, G. H., Groppi, C. E., Alonso-Herrero, A., Rieke, M. J., & Engelbracht, C. W. 2000, *ApJ*, 545, 190
- Jungwiert, B., & Palous, J. 1996, *A&A*, 311, 397
- Kenney, J. D. P. 1996, in *Barred Galaxies*, ed. R. Buta, D. A. Crocker, & B. G. Elmegreen (San Francisco, ASP), 150
- Kenney, J. D. P., Carlstrom, J. E., & Young, J. S. 1993, *ApJ*, 418, 687
- Kenney, J. D. P., & Load, S. D. 1991, *ApJ*, 381, 118
- Kenney, J. D. P., Wilson, C. D., Scoville, N. Z., Devereux, N. A., & Young, J. S. 1992, *ApJ*, 395, L79
- Knapen, J. H., Shlosman, I., & Peletier, R. F. 2000, *ApJ*, 529, 93
- Koda, J., Sofue, Y., Kohno, K., Nakanishi, H., Onodera, S., Okumura, S.K., & Irwin, J. A. 2002, *ApJ*, 573, 105
- Kohno, K., Kawabe, R., & Vila-Vilaró, B. 1999a, *ApJ*, 511, 157
- Kohno, K., Kawabe, R., & Vila-Vilaró, B. 1999b, in *The Physics and Chemistry of the Interstellar Medium*, ed. V. Ossenkopf, J. Stutzki, & G. Winnewisser (Herdecke, GCA-Verlag), 34 (astro-ph/9902251)
- Kohno, K., Matsushita, S., Vila-Vilaró, B., Okumura, S. K., Shibatsuka, T., Okiura, M., Ishizuki, S., & Kawabe, R. 2001, in *The Central Kiloparsec of Starbursts and AGN: The La Palma Connection*, ed. J. H. Knapen, J. E. Beckman, I. Shlosman, & T. J. Mahoney (San Francisco, ASP), 672 (astro-ph/0206398)
- Kormendy, J., & Richstone, D. 1995, *ARA&A*, 33, 581
- Koratkar, A., Deustua, S. E., Heckman, T., Filippenko, A. V., Ho, L. C., & Rao, M. 1995, *ApJ*, 440, 132
- Kuno, N., Nishiyama, K., Nakai, N., Sorai, K., Vila-Vilaó, B., & Handa, T. 2000, *PASJ*, 52, 775
- Laine, S., Shlosman, I., Knapen, J. H., & Peletier, R. F. 2002, *ApJ*, 567, 97
- Maiolino, R., Alonso-Herrero, A., Anders, S., Quillen, A., Rieke, M. J., Rieke, G. H., & Tacconi-Garman, L. E. 2000, *ApJ*, 531, 219
- Maiolino, R., Krabbe, A., Thatte, N., & Genzel, R. 1998, *ApJ*, 493, 650
- Maiolino, R., Ruiz, M., Rieke, G. H., & Papadopoulos, P. 1997, *ApJ*, 485, 552
- Martini, P., & Pogge, R. W. 1999, *AJ*, 118, 2646
- McLeod, K. K., & Rieke, G. H. 1995, *ApJ*, 441, 96
- Mulchaey, J. S., & Regan, M. W. 1997, *ApJ*, 482, L135
- Mulchaey, J. S., Regan, M. W., & Kundu, A. 1997, *ApJS*, 110, 299
- Nakai, N. 1992, *PASJ*, 44, L27
- Nakai, N., & Kuno, N. 1995, *PASJ*, 47, 761
- Nishiyama, K., & Nakai, N. 2001, *PASJ*, 53, 713
- Nishiyama, K., Nakai, N., & Kuno, N. 2001, *PASJ*, 53, 757
- Oka, T., Hasegawa, T., Hayashi, M., Handa, T., & Sakamoto, S. 1998, *ApJ*, 493, 730
- Papadopoulos, P. P., & Seaquist, E. R. 1998, *ApJ*, 492, 521
- Peletier, R. F., Knapen, J. H., Shlosman, I., Pérez-Ramírez, D., Nadeau, D., Doyon, R., Rodríguez-Espinosa, J. M., & García, A. M. P. 1999, *ApJS*, 125, 363
- Quillen, A. C., McDonald, C., Alonso-Herrero, A., Lee, A., Shaked, S., Rieke, M.J., & Rieke, G.H. 2001, *ApJ*, 547, 129
- Rees, M. J. 1984, *ARA&A*, 22, 471
- Regan, M. W. 2000, *ApJ*, 541, 142
- Regan, M. W., & Mulchaey, J. S. 1999, *AJ*, 117, 2676
- Regan, M. W., Sheth, K., & Vogel, S. N. 1999, *ApJ*, 526, 97
- Reynaud, D., & Downes, D. 1998, *A&A*, 337, 671
- Robert, S. W. Jr., Huntley, J. M., & van Albada, G. D. 1979, *ApJ*, 233, 67
- Rush, B., Malkan, M.A., & Spinoglio, L. 1993, *ApJS*, 89, 1
- Sakamoto, K., Baker, A. J., & Scoville, N. Z. 2000, *ApJ*, 533, 149
- Sakamoto, K., Okumura, S. K., Ishizuki, S., & Scoville, N. Z. 1999a, *ApJS*, 124, 403
- Sakamoto, K., Okumura, S. K., Ishizuki, S., & Scoville, N. Z. 1999b, *ApJ*, 525, 691
- Sakamoto, K., Okumura, S., Minezaki, T., Kobayashi, Y., & Wada, K. 1995, *AJ*, 110, 2075
- Sandage, A., & Tammann, G. A. 1981, *A Revised Sharpley-Ames Catalog of Bright Galaxies* (Washington, Carnegie Institution of Washington)
- Schinnerer, E., Eckart, A., Tacconi, L. J., Genzel, R., & Downes, D. 2000, *ApJ*, 533, 850
- Scoville, N. Z., Matthews, K., Carico, D. P., & Sanders, D. B. 1988, *ApJ*, 327, L61
- Sempere, M.J., García-Burillo, S., Combes, F., & Knapen, J. H. 1995, *A&A*, 296, 45
- Shlosman, I., Frank, J., & Begelman, M. C. 1989, *Nature*, 338, 45
- Sofue, Y. 1997, *PASJ*, 49, 17
- Solomon, P. M., Downes, D., Radford, S. J. E., & Barrett, J. W. 1997, *ApJ*, 478, 144

- Sorai, K., Nakai, N., Kuno, N., Nishiyama, K., & Hasegawa, T. 2000, PASJ, 52, 785
- Stark, A. A., Elmegreen, B. G., & Chance, D. 1987, ApJ, 322, 64
- Storchi-Bergmann, T., González Delgado, R. M., Schmitt, H. R., Cid Fernandes, R., & Heckman, T. 2001, ApJ, 559, 147
- Telesco, C. M., Dressel, L. L., & Wolstencroft, R. D. 1993, ApJ, 414, 120
- Terashima, Y., Kunieda, H., & Misaki, K. 1999, PASJ, 51, 277
- Thean, A. H. C., Mundell, C. G., Pedlar, A., & Nicholson, R. A. 1997, MNRAS, 290, 15
- Thronson, H. A., Hereld, M., Majewski, S., Greenhouse, M., Johnson, P., Spillar, E., Woodward, C. E., et al. 1989, ApJ, 343, 158
- Tsutsumi, T., Morita, K. -I., & Umeyama, S. 1997, in Astronomical Data Analysis Software and Systems VI, ed. G. Hunt, H.E. Payne (San Francisco, ASP), 50
- Tully, R. 1988, Nearby Galaxies Catalog (Cambridge University Press, Cambridge)
- Ulvestad, J. S., & Wilson, A. S. 1989, ApJ, 343, 659
- van der Marel, R. P. 1999, AJ, 117, 744
- Vila-Vilaró, B., Taniguchi, Y., & Nakai, N. 1998, AJ, 116, 1553
- Wada, K., & Habe, A. 1992, MNRAS, 258, 82
- Wada, K., & Norman, C. A. 2002, ApJ, 566, L21
- Wevers, B. M. H. R., van der Kruit, P. C., & Allen, R. J. 1986, A&AS, 66, 505
- Wong, T., & Blitz, L. 2002, ApJ, 569, 157
- Yamashita, T., Nishihara, E., Okumura, S., Mori, A., & Watanabe, E. 1995, in Scientific and Engineering Frontiers for 8-10m Telescopes – Instrumentation for Large Telescopes in the 21st Century, ed. M. Iye, & T. Nishimura (Tokyo, Universal Academy Press), 285
- Young, J.S., Xie, S., Tacconi, L., Knezek, P., Viscuso, P., Tacconi-Garman, L., Scoville, N., et al. 1995, ApJS, 98, 219

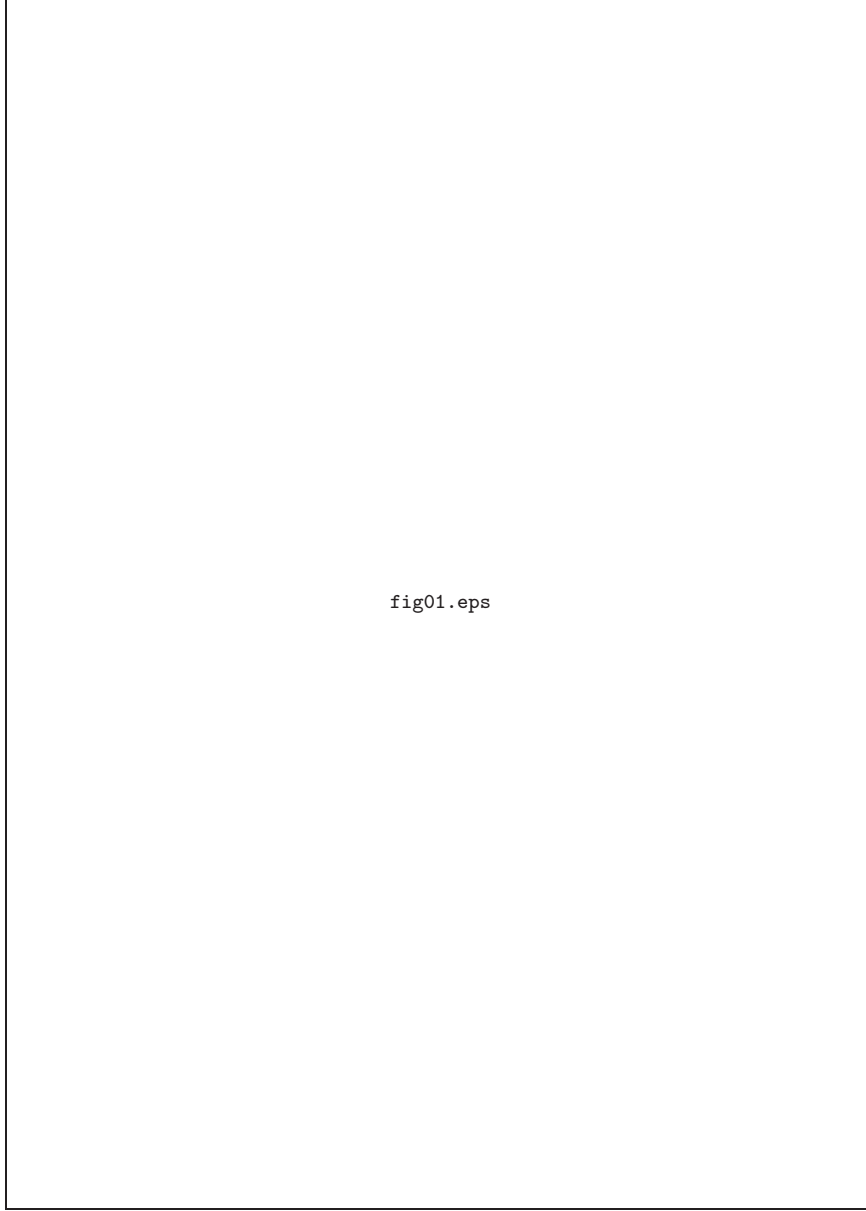


**Fig. 1.** Channel maps of CO(1–0) emission from the central  $45'' \times 75''$  region ( $4.1 \text{ kpc} \times 6.8 \text{ kpc}$  at  $D = 18.7 \text{ Mpc}$ ) of NGC 5033. Velocity channels with a width of  $19.55 \text{ km s}^{-1}$  are displayed at an interval of  $9.78 \text{ km s}^{-1}$ . The central velocity ( $V_{\text{LSR}}$  in  $\text{km s}^{-1}$ ) of each channel is labeled. The size of the synthesized beam is  $3.''9 \times 3.''6$  (HPBW), shown as an ellipse. The contour levels are  $-4, -2, 2, \dots, 12\sigma$ , where  $1 \sigma = 30 \text{ mJy beam}^{-1}$  or  $200 \text{ mK}$  in  $T_{\text{b}}$ . The large cross indicates the position of the  $6 \text{ cm}$  radio continuum peak, and the small cross shows the pointing center. The circle represents the field of view ( $65''$ ). The attenuation due to the primary beam pattern is not corrected in these maps.



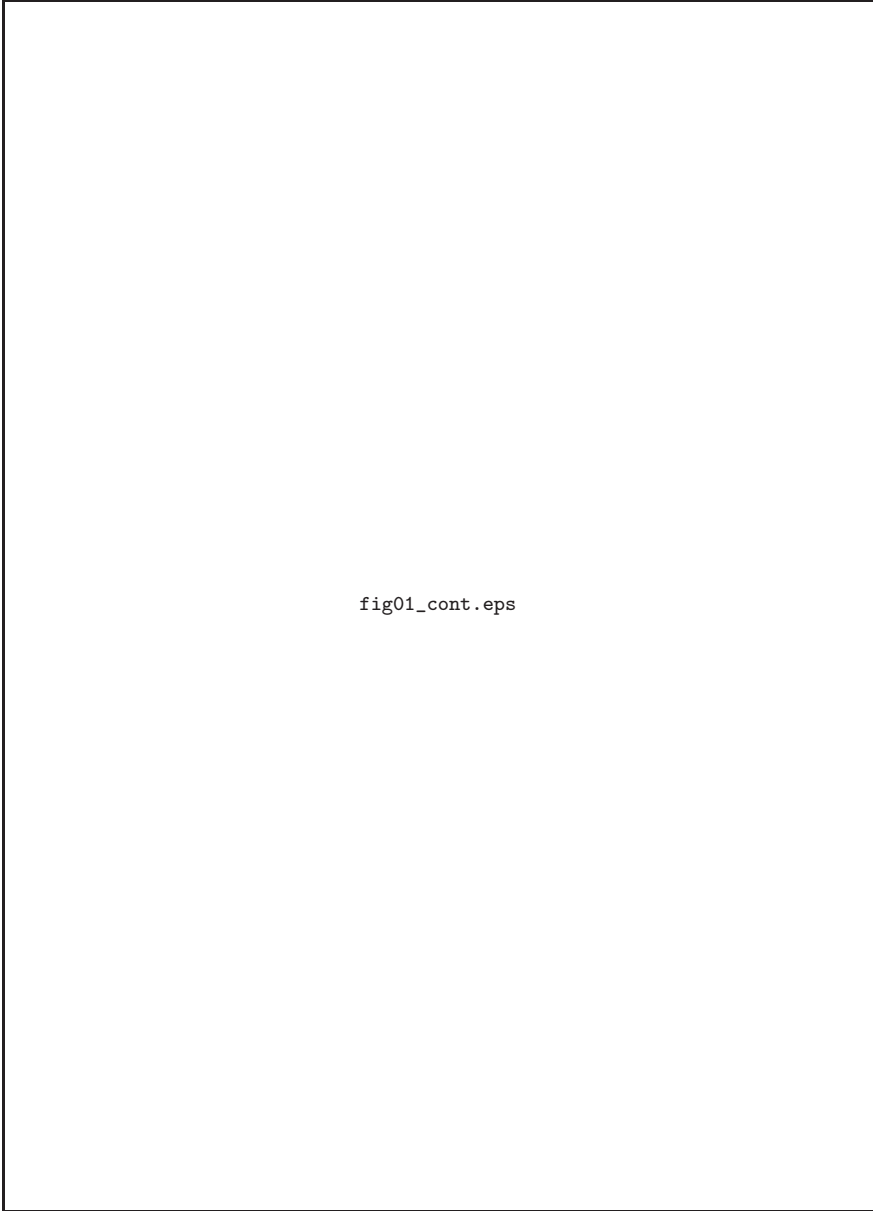


**Fig. 1.** (Continued)



**Fig. 2.** (a) Optical image of NGC 5033 from the Digitized Sky Survey, showing a  $3' \times 6'$  ( $16 \text{ kpc} \times 33 \text{ kpc}$  at  $D = 18.7 \text{ Mpc}$ ) field around the center of NGC 5033. (b) Integrated intensity map of the CO(1–0) emission over a velocity range from  $V_{\text{LSR}} = 651.5$  to  $1119.4 \text{ km s}^{-1}$  in the central  $45'' \times 75''$  ( $4.1 \text{ kpc} \times 6.8 \text{ kpc}$ ) region of NGC 5033. The synthesized beam,  $3''9 \times 3''6$  with a *P.A.* of  $6^\circ$ , is shown as an ellipse in a box. The contour levels are 1.5, 3, 4.5,  $\dots$ ,  $13.5 \sigma$ , where  $1\sigma = 2.0 \text{ Jy beam}^{-1} \text{ km s}^{-1}$  or  $13 \text{ K km s}^{-1}$  in  $T_{\text{b}}$ . The  $1\sigma$  level corresponds to the face-on molecular gas (including He and heavier elements) surface density  $\Sigma_{\text{gas}} = 23 M_{\odot} \text{ pc}^{-2}$ . The large cross indicates the position of the 6 cm radio continuum peak [ $\alpha$  (B1950) =  $13^{\text{h}}11^{\text{m}}09^{\text{s}}23$ ,  $\delta$  (B1950) =  $+36^\circ51'30''27$ ], and the small cross indicates the phase center of the observations. The circle represents the field of view (HPBW of the primary beam,  $65''$ ). Attenuation due to the primary beam pattern is corrected in this map. Note that the peak of CO emission is not located at the Seyfert nucleus. (c) Intensity-weighted mean velocity map of CO emission in the central  $45'' \times 75''$  region ( $4.1 \text{ kpc} \times 6.8 \text{ kpc}$  at  $D = 18.7 \text{ Mpc}$ ) of NGC 5033. The contour interval is  $20 \text{ km s}^{-1}$ , and the systemic velocity,  $V_{\text{LSR}} = 882 \text{ km s}^{-1}$ , is indicated by a black contour.

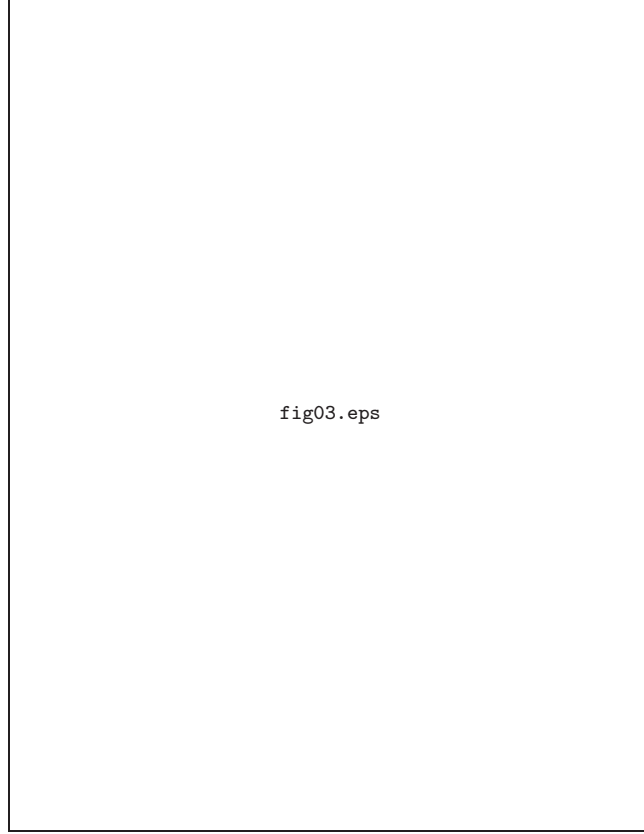


**Fig. 3.** Integrated intensity map of the CO(1-0) emission over a velocity range from  $V_{\text{LSR}} = 651.5$  to  $1119.4 \text{ km s}^{-1}$  in the central  $45'' \times 75''$  region ( $4.1 \text{ kpc} \times 6.8 \text{ kpc}$  at  $D = 18.7 \text{ Mpc}$ ) of NGC 5033. Part of the molecular ring and spirals are indicated as thick lines.

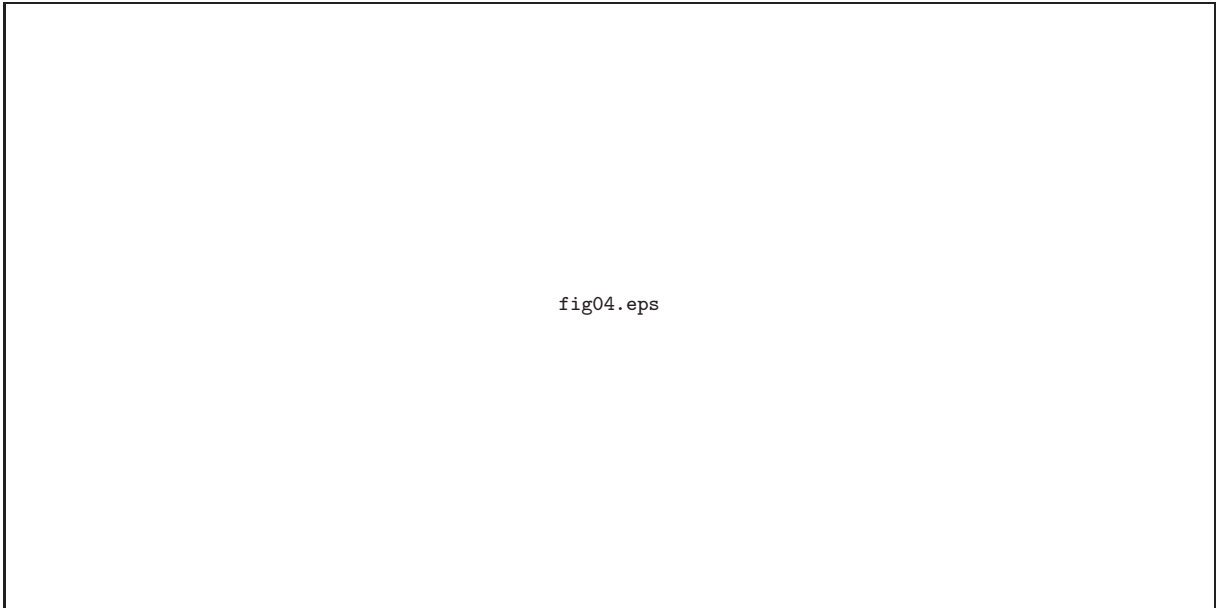


**Fig. 4.** CO spectra from the central  $21'' \times 21''$  region of NGC 5033. The spectra were measured from the NMA data cube at  $7 \times 7$  points on a  $3''$  spacing grid with respect to the major axis ( $P.A. = -8^\circ$ ). The grid positions are indicated as crosses on the integrated intensity map. The contour levels of the CO map are 2, 5, 8, and  $11 \sigma$  where  $1 \sigma = 2.0 \text{ Jy beam}^{-1} \text{ km s}^{-1}$  or  $13 \text{ K km s}^{-1}$  in  $T_b$ . This CO map is rotated by  $8^\circ$  counter clockwise. The velocity bin of the spectra is  $9.78 \text{ km s}^{-1}$ . The primary beam attenuation is corrected. The noise level near the central position is  $30 \text{ mJy beam}^{-1}$  or  $200 \text{ mK}$  in  $T_b$ . Very broad and double-peaked CO profiles are evident near the (0, 3) and (0, -3) positions, which correspond to the two CO peaks in the map.

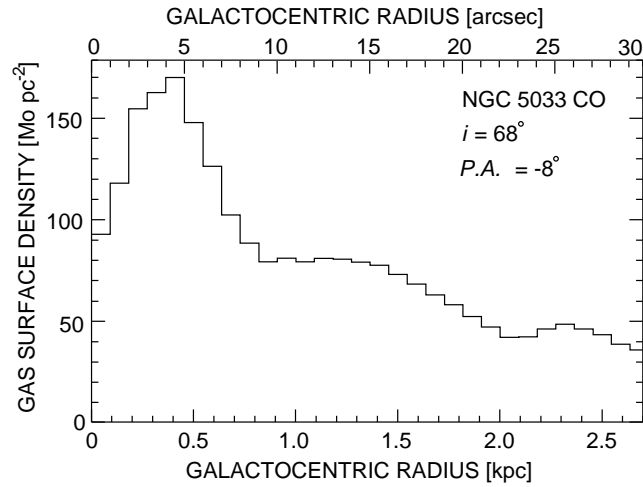


**Fig. 5.** Radial distribution of the molecular gas surface density in NGC 5033. The CO intensities corrected to face-on were azimuthally averaged over the successive annuli with  $1'' = 90.7$  pc.  $X_{\text{CO}} = 1.8 \times 10^{20} \text{ cm}^{-2} (\text{K km s}^{-1})^{-1}$  was adopted to compute the gas surface density. This surface density includes heavy elements as  $1.36 \times \Sigma_{\text{H}_2}$ . The maximum of gas surface density is located at a radius of  $\sim 400$  pc, not at the center. The second peak is also seen at  $r \sim 14''$  or 1.3 kpc.

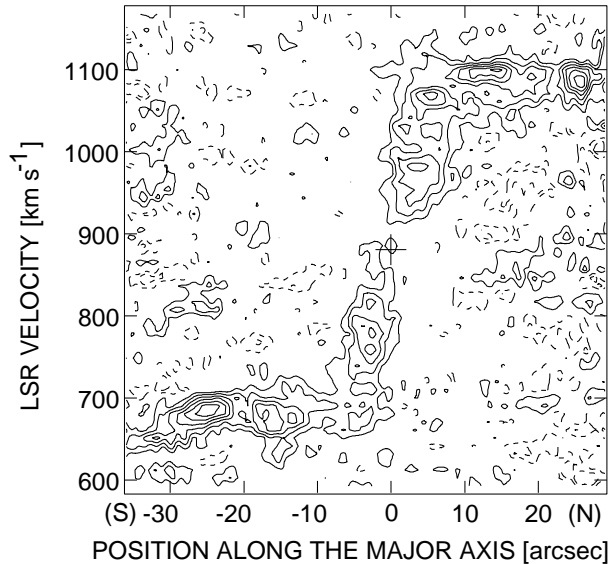


**Fig. 6.** Position – velocity map (P–V map) of the CO emission along the major axis of NGC 5033 ( $P.A. = -8^\circ$ ). Contour levels are  $-3, -1.5, 1.5, \dots, \text{and } 9 \sigma$ , where  $1 \sigma = 30 \text{ mJy beam}^{-1}$  or  $200 \text{ mK}$  in  $T_{\text{b}}$ . Negative contours are dashed. The primary beam correction is applied. The cross indicates the kinematical center [ $\alpha$  (B1950) =  $13^{\text{h}}11^{\text{m}}09^{\text{s}}23$ ,  $\delta$  (B1950) =  $+36^\circ51'29''9$ , and  $V_{\text{sys}} = 882 \text{ km s}^{-1}$ ].



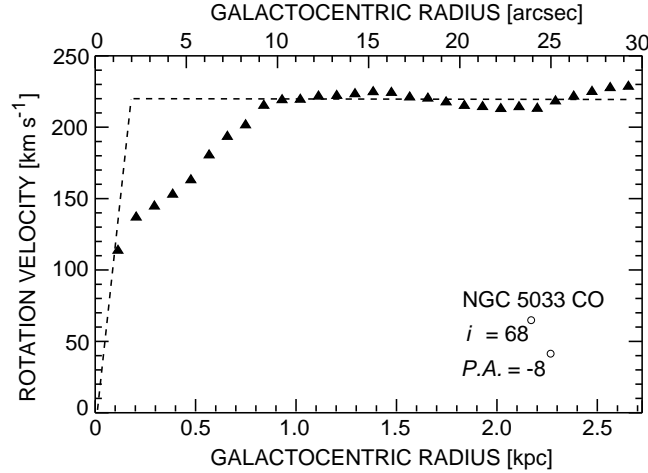


**Fig. 7.** Circular rotation curve of NGC 5033. This is derived from the intensity-weighted mean velocity map of the CO emission within  $\pm 5^\circ$  of the major axis. Inclination ( $68^\circ$ ) is corrected. Note that a gradual rise in the rotation velocity near the center ( $r < 10''$ ) could be due to a smearing of the observing beam and multiple velocity components near the center due to a bar, and the true rotation velocity must be larger there, as can be seen in the P-V diagram (figure 6). In the following analysis, we assume a constant rotation velocity of  $220 \text{ km s}^{-1}$  for  $r > 2''$ , and a rigid-body rotation of  $\Omega = 1.2 \text{ km s}^{-1} \text{ pc}^{-1}$  for  $r < 2''$ , as indicated by dashed lines.

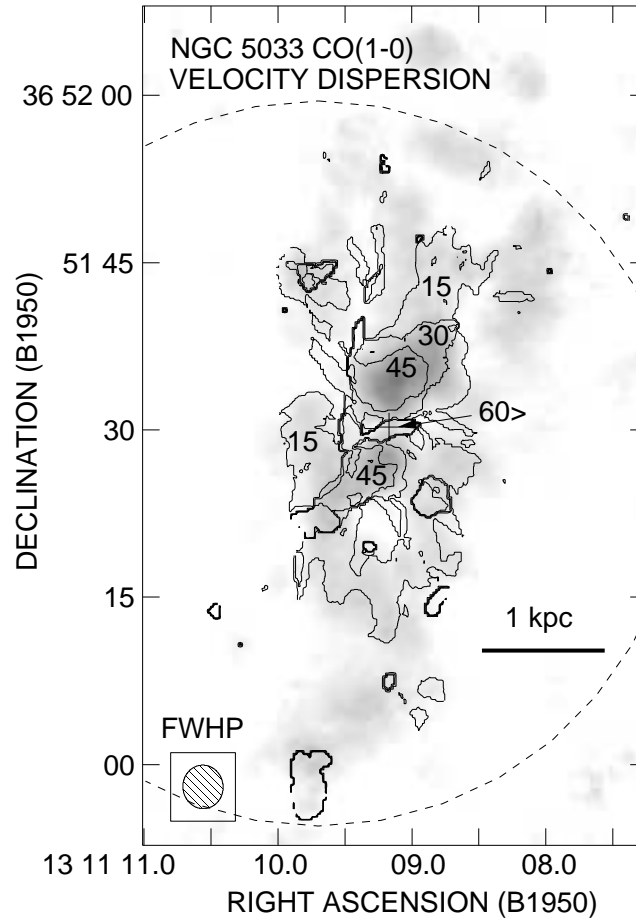


**Fig. 8.** Intensity-weighted velocity dispersion map of the CO emission. The contour interval is  $15 \text{ km s}^{-1}$ . This map is computed by calculating the second-order moment of intensity at each point from the CO cube. The cross shows the position of the 6 cm radio nucleus, and the dashed circle represents the field of view (HPBW of the primary beam), that is  $65''$  diameter. Large velocity dispersions near the two CO peaks,  $\sigma_v > 40 \text{ km s}^{-1}$ , are evident. This map contains both the intrinsic velocity dispersion of gas and the gradient of rotation velocity in the observed beam.

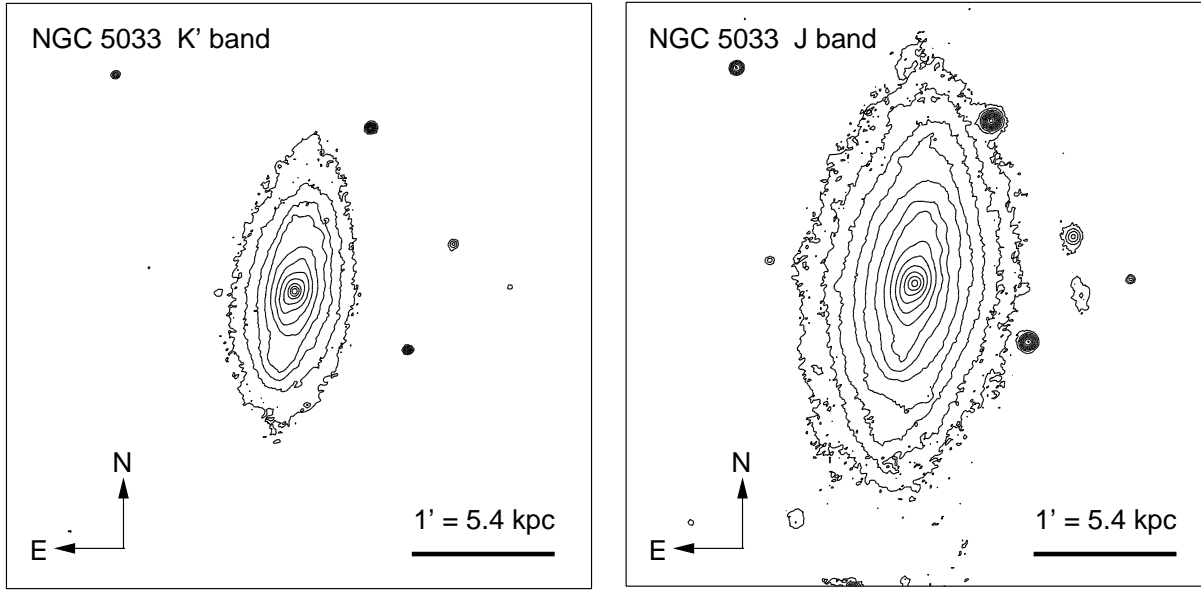


**Fig. 9.** Near-infrared images of NGC 5033 in a field of  $4'.1 \times 4'.1$  (22.3 kpc square). The contour levels are 18.0, 17.5, 17.0, ..., 13.0 mag arcsec $^{-2}$  for  $K'$  the band, and 20.5, 20.0, 19.5, ..., 14.5 mag arcsec $^{-1}$  for the  $J$  band. The horizontal bars indicate the  $1'$  or 5.44 kpc at  $D = 18.7$  Mpc. The seeing size is about  $1''.7$  for the  $K'$  band and  $3''.2$  for the  $J$  band, respectively.

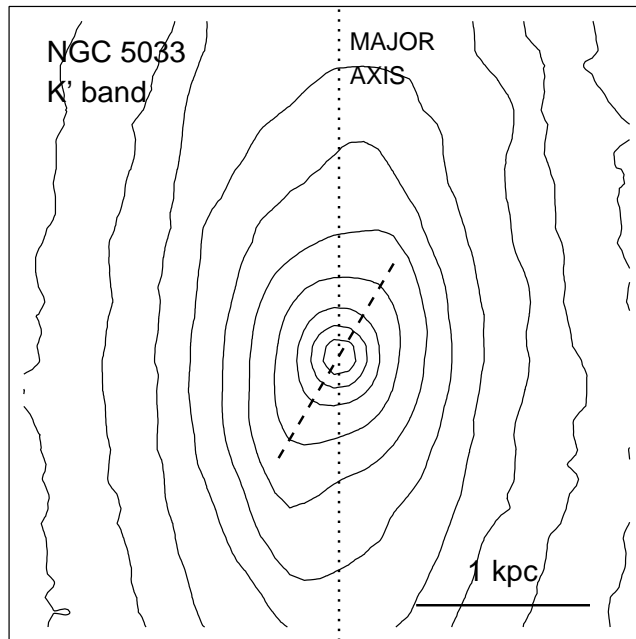


**Fig. 10.** Central  $40'' \times 40''$  area in  $K'$  band. The contour levels are same as in figure 9. This map is rotated by  $8^\circ$  counter clockwise. The major axis is denoted as the dotted line. There exists a possible shift of the isophotal contours near the center, as indicated by the short dashed line.

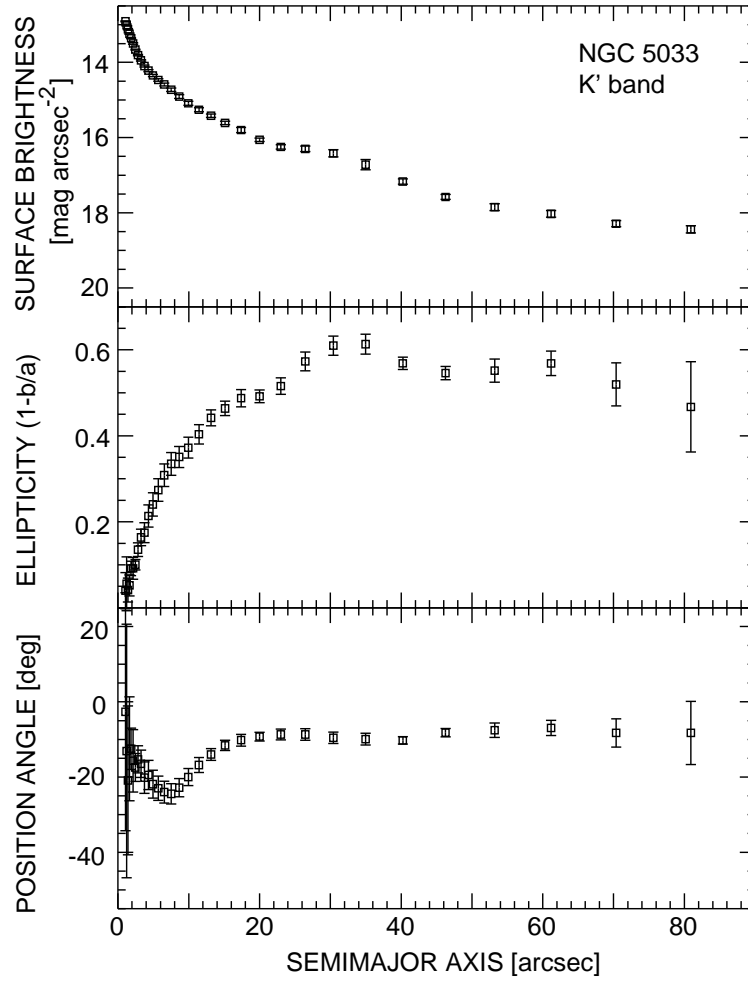


**Fig. 11.** Mean surface brightness, ellipticity ( $1 - b/a$ ), and position angle (North is  $0^\circ$ , and West is  $-90^\circ$ ) as a function of the semimajor axis radius of elliptical isophots fitting for the  $K'$  band image of NGC 5033. The error bars are  $\pm 1 \sigma$ .



**Fig. 12.**  $J - K'$  color index image (left), and the comparison of the color index with the integrated CO distribution (right) in the central  $2'.05 \times 2'.05$  region of NGC 5033. Gray-scale ranges from 0.5 to 1.5 mag (whiter is redder), and contour levels are 2, 4, 6,  $\dots$ , 12  $\sigma$ , where  $1\sigma = 2.0 \text{ Jy beam}^{-1} \text{ km s}^{-1}$  or  $13 \text{ K km s}^{-1}$  in  $T_b$ . A circumnuclear ring with a diameter of  $\sim 1.3 \text{ kpc}$  and two spiral arms are clearly depicted, and the CO distribution agrees with the ring and two spirals.

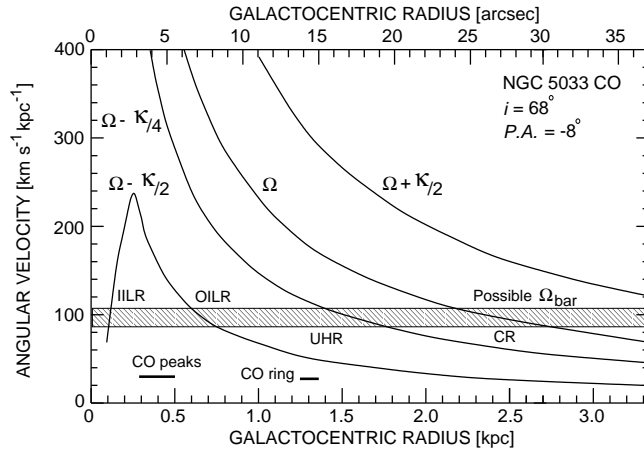


**Fig. 13.** Angular velocities ( $\Omega$ ,  $\Omega \pm \kappa/2$ , and  $\Omega - \kappa/4$ ) as a function of galactocentric radius, assuming the CO circular rotation curve discussed in subsection 3.1.6. A proposed range of the nuclear bar pattern speeds ( $\Omega_{\text{bar}}$ ) is shown, which is derived by assuming the corotation resonance lies at the observed cut off radius of the molecular gas (i.e.,  $R_{\text{CR}} = 2.7 \text{ kpc}$ ) or at the local dip radius of the CO radial distribution in figure 5 (i.e.,  $R_{\text{CR}} = 2.1 \text{ kpc}$ ). This diagram suggests that the CO ring at  $r \sim 1.3 \text{ kpc}$  corresponds to the UHR, and the CO twin peaks and ridges occur between IILR and OILR.



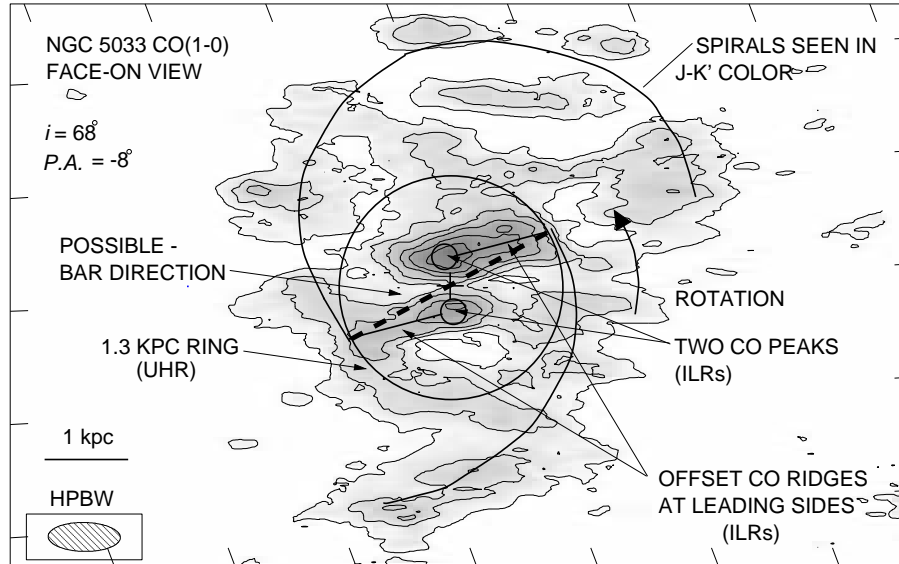


**Fig. 14.** Face-on view of the integrated CO intensity map in NGC 5033 (figure 3), corrected the inclination of the galactic disk. The abscissa is aligned to the minor axis of the galaxy,  $P.A. = 82^\circ$ . The thick lines trace the molecular offset-ridges, ring, and spirals structures. These observed CO features are well understood as a response to the nuclear bar (indicated by the dashed line across the nucleus).

Table 1. Properties of NGC 5033.

Parameter	Value	Reference*
Morphology .....	SA(s)c	(1)
	Sbc(s)I-II	(2)
Nuclear activity .....	Type 1.5 Seyfert	(3)
Position of nucleus:		(4)
$\alpha$ (B1950) .....	13 <sup>h</sup> 11 <sup>m</sup> 09 <sup>s</sup> 171	
$\delta$ (B1950) .....	+36°51'30''27	
$D_{25} \times d_{25}$ .....	10'.7 $\times$ 5'.0	(1)
Position angle .....	-8° (North = 0°, West = -90°)	(5)
Inclination angle .....	68° (edge-on = 90°)	(5)
Systemic velocity (LSR) .....	870 km s <sup>-1</sup>	(5)
Adopted distance .....	18.7 Mpc	(6)
Linear scale .....	90.7 pc arcsec <sup>-1</sup>	

\* (1) de Vaucouleurs et al. 1991 (RC3); (2) Sandage, Tammann 1987 (RSA); (3) Ho et al. 1997a; (4) Ulvestad, Wilson 1989; (5) Thean et al. 1997; (6) Tully, 1988.

Table 2. NMA Observations of NGC 5033.

Parameter	Value
Observations period .....	1993 Dec. – 1994 Apr., 1996 Jan.
Phase center:	
$\alpha$ (B1950) .....	13 <sup>h</sup> 11 <sup>m</sup> 09 <sup>s</sup> .7
$\delta$ (B1950) .....	+36°51'27''0
Visibility calibrator .....	1308+326
Line .....	CO( $J = 1-0$ )
Rest frequency .....	115.271204 GHz
Observed frequency .....	114.928 GHz
Array configuration .....	AB, C, and D
Projected baseline .....	3.8 – 142 $k\lambda$ or 10 – 370 m
Field of view .....	65'' or 5.9 kpc
Band width .....	319.815680 MHz
Velocity coverage .....	836 km s <sup>-1</sup>
Velocity resolution .....	9.78 km s <sup>-1</sup>
Synthesized beam .....	3''.9 $\times$ 3''.6, $P.A.$ 6° or 350 $\times$ 330 pc
Equivalent $T_b$ for 1 Jy beam <sup>-1</sup> .....	6.6 K
r.m.s. noise in channel maps .....	30 mJy beam <sup>-1</sup> or 200 mK in $T_b$

Table 3. Kinematical parameters derived from the CO velocity field.

Parameter	Value
Kinematical center:	
$\alpha$ (B1950) .....	13 <sup>h</sup> 11 <sup>m</sup> 09 <sup>s</sup> 23 $\pm$ 0 <sup>s</sup> .083
$\delta$ (B1950) .....	+36°51'29''9 $\pm$ 1''
Position angle .....	-7°5 $\pm$ 1°
Inclination angle .....	66° $\pm$ 3°
Systemic velocity .....	882 km s <sup>-1</sup> $\pm$ 5 km s <sup>-1</sup>

This figure "fig01.png" is available in "png" format from:

<http://arxiv.org/ps/astro-ph/0301417v1>

This figure "fig01\_cont.png" is available in "png" format from:

<http://arxiv.org/ps/astro-ph/0301417v1>

This figure "fig02.png" is available in "png" format from:

<http://arxiv.org/ps/astro-ph/0301417v1>

This figure "fig03.png" is available in "png" format from:

<http://arxiv.org/ps/astro-ph/0301417v1>

This figure "fig04.png" is available in "png" format from:

<http://arxiv.org/ps/astro-ph/0301417v1>



This figure "fig12.jpg" is available in "jpg" format from:

<http://arxiv.org/ps/astro-ph/0301417v1>